

Dual-energy computed tomography to assess intra- and inter-patient tissue variability for proton treatment planning of brain-tumor patients

Wohlfahrt, P.; Möhler, C.; Troost, E.; Greilich, S.; Richter, C.;

Originally published:

July 2019

Radiotherapy and Oncology 105(2019)3, 504-513

DOI: <https://doi.org/10.1016/j.ijrobp.2019.06.2529>

Perma-Link to Publication Repository of HZDR:

<https://www.hzdr.de/publications/Publ-27917>

Release of the secondary publication
on the basis of the German Copyright Law § 38 Section 4.

CC BY-NC-ND

1 **TITLE: Dual-energy computed tomography to assess intra- and inter-patient tissue**
2 **variability for proton treatment planning of brain-tumor patients**

3
4 **SHORTENED RUNNING TITLE: DECT-based tissue variability assessment**

5
6 **Authors:** Patrick Wohlfahrt^{*,†}, Christian Möhler^{‡,§}, Esther G. C. Troost^{*,†,||,¶,#},
7 Steffen Greilich^{‡,§}, Christian Richter^{*,†,||,¶}

8
9 **Institutions:**

10 * OncoRay - National Center for Radiation Research in Oncology, Faculty of Medicine and
11 University Hospital Carl Gustav Carus, Technische Universität Dresden, Helmholtz-Zentrum
12 Dresden - Rossendorf, Dresden, Germany

13 † Helmholtz-Zentrum Dresden - Rossendorf, Institute of Radiooncology - OncoRay, Dresden,
14 Germany

15 ‡ German Cancer Research Center (DKFZ), Heidelberg, Germany

16 § National Center for Radiation Research in Oncology (NCRO), Heidelberg Institute for
17 Radiation Oncology (HIRO), Heidelberg, Germany

18 || Department of Radiotherapy and Radiation Oncology, Faculty of Medicine and University
19 Hospital Carl Gustav Carus, Technische Universität Dresden, Dresden, Germany

20 ¶ German Cancer Consortium (DKTK), Partner Site Dresden, Germany

21 # National Center for Tumor Diseases (NCT), Partner Site Dresden, Germany: German
22 Cancer Research Center (DKFZ), Heidelberg, Germany; Faculty of Medicine and University
23 Hospital Carl Gustav Carus, Technische Universität Dresden, Dresden, Germany, and;
24 Helmholtz Association / Helmholtz-Zentrum Dresden - Rossendorf, Dresden, Germany

25
26 **Corresponding author:** Patrick Wohlfahrt, PhD, OncoRay - National Center for Radiation
27 Research in Oncology, Faculty of Medicine and University Hospital Carl Gustav Carus,
28 Technische Universität Dresden, Helmholtz-Zentrum Dresden - Rossendorf, Dresden,
29 Germany, Tel. +49 351 458 7626, E-mail: Patrick.Wohlfahrt@OncoRay.de

30
31 **Keywords:** dual-energy CT; tissue variability; proton therapy

32

33	Total number of pages:	26
34	Number of tables:	0
35	Number of figures:	6

36 **ABSTRACT:**

37 **Background and Purpose:**

38 Range prediction in particle therapy is associated with an uncertainty originating from the
39 calculation of stopping-power ratio (SPR) based on x-ray computed tomography (CT). Here,
40 we assessed the intra- and inter-patient variability of tissue properties in primary brain-tumor
41 patients using dual-energy CT (DECT) and quantified its influence on current SPR prediction.

42

43 **Material and Methods:**

44 Based on 102 patient DECT scans, SPR distributions were derived from a patient-specific
45 DECT-based approach. Tissue-specific and global deviations between this method and the
46 state-of-the-art CT-number-to-SPR conversion applying a Hounsfield look-up table (HLUT)
47 were quantified. To isolate systematic deviations between both, the HLUT was optimized
48 using DECT. Subsequently, the influence of soft tissue diversity and age-related variations in
49 bone composition on SPR were assessed.

50

51 **Results:**

52 An intra-patient \pm inter-patient soft tissue diversity of $(4.4\pm 0.7)\%$ in SPR was obtained after
53 conservative consideration of noise-induced variation. Between adults and children younger
54 than 6 years, age-related variations in bone composition resulted in a median SPR difference
55 of approximately 5%.

56

57 **Conclusions:**

58 Patient-specific DECT-based stopping-power prediction can intrinsically incorporate most of
59 the SPR variability arising from tissue mixtures, inter-patient and intra-tissue variations. Since
60 the state-of-the-art HLUT - even after cohort-specific optimization - cannot fully consider the

61 broad tissue variability, patient-specific DECT-based stopping-power prediction is advisable
62 in particle therapy.

63 **MANUSCRIPT:**

64 **Introduction**

65 To facilitate accurate and high-conformal radiation treatment planning, a reliable
66 determination of the individual tissue compositions of each patient is worthwhile [1].
67 Especially in proton and ion-beam therapy, a precise range prediction from x-ray computed
68 tomography (CT) is essential to translate the particle beam's physical advantage into a further
69 improved clinical outcome [2–4].

70 The current acquisition of single-energy CT scans and their conversion from CT number to
71 stopping-power ratio (SPR) using a generic Hounsfield look-up table (HLUT) are restricted to
72 specific material compositions and cannot adequately account for tissue diversity [5,6]. The
73 associated CT-related uncertainty of range calculation is covered by considerable safety
74 margins added in beam direction or is incorporated in robust optimization techniques leading
75 to an increased dose to healthy tissue, which is worth to be reduced [7–10]. Since there are
76 substantial intra- and inter-patient variations in elemental composition of human tissues [5],
77 appropriate and adequately commissioned imaging techniques are desirable to accurately
78 quantify the respective tissue distribution and variability.

79 With the advent of clinical dual-energy CT (DECT) scanners in radiology and radiotherapy,
80 additional tissue information can be obtained from two CT scans of different x-ray spectra
81 allowing for a better material differentiation compared with single-energy CT [11,12]. Hence,
82 the clinical application of DECT for proton treatment planning [13] is expected to inherently
83 incorporate most of intra- and inter-patient tissue variability in a patient-specific SPR
84 prediction [14–16], since the empirical component in CT-based SPR calculation is strongly
85 mitigated. In recently published studies, the reliability and superior accuracy of DECT-based
86 SPR prediction as an alternative to the current state-of-the-art application of a generic HLUT
87 were demonstrated under clinical conditions in an anthropomorphic head phantom [17] and in
88 biological tissue samples [18–20], and finally transferred to relative range shifts obtained in

89 patients [21,22]. Consequently, DECT can presumably contribute to a reduction of the CT-
90 related range uncertainty and associated safety margins.

91 In this study, DECT scans acquired for proton treatment planning of 102 primary brain-tumor
92 patients were retrospectively evaluated to assess the intra- and inter-patient variability of CT-
93 based SPR prediction originating from various tissue types, tissue mixtures and intra-tissue
94 variations.

95

96 **Material and Methods**

97 *Patient cohort and DECT imaging*

98 In total, 102 primary brain-tumor patients (40 women, 40 men and 22 children younger than
99 20 years) treated with proton therapy at OncoRay (Dresden, Germany) were selected covering
100 a wide range of brain-tumor entities (36 glioblastoma, 25 astrocytoma, 13 meningioma,
101 9 sarcoma, 7 adenoma, 7 glioma, 2 craniopharyngioma, 2 ependymoma and 1 germinoma)
102 and patient age (1-80 years, median age of 45 years). This retrospective study was approved
103 by the local ethics committee (EK535122015).

104 For each patient, a DECT scan (80/140 kVp) with $1 \times 1 \times 2 \text{ mm}^3$ voxel spacing and
105 $\text{CTDI}_{\text{vol}32\text{cm}}$ of 20.8 mGy was acquired at a single-source CT scanner SOMATOM Definition
106 AS (Siemens Healthineers, Forchheim, Germany) [13]. Image reconstruction was performed
107 using the iterative reconstruction kernel Q34f/5 (SAFIRE at maximal strength), which
108 includes a beam hardening correction for bone, to reduce image noise and patient-size
109 dependent CT number variations. An image noise level (CT number variation expressed by
110 \pm two standard deviations) of 5 HU was determined for this scan setting in a homogeneous
111 brain region of an anthropomorphic head phantom (Proton Therapy Dosimetry Head, Model
112 731-HN, CIRS, Inc., Norfolk, VA).

113

114

115 *Tissue parameter extraction*

116 The DECT scans were post-processed in the SYNGO.VIA environment (Siemens Healthineers,
117 Forchheim, Germany) to calculate 79 keV pseudo-monoenergetic CT (MonoCT), 170 keV
118 MonoCT and effective atomic number (EAN) datasets using the modules SYNGO.CT DE
119 MONOENERGETIC PLUS and SYNGO.CT DE RHO/Z. Based on an individual CT scanner
120 calibration [13], the relative electron density (RED) was obtained from 170 keV MonoCT
121 datasets. Dividing 79 keV MonoCT by RED resulted in the relative photon attenuation cross
122 section (RCS). Both quantities are then inserted in the Bethe equation [23] to directly
123 determine the SPR (DirectSPR). This approach, referred to as RhoSigma [16], was
124 implemented as described in [17,21]. An image noise level of 6 HU (corresponding to two
125 standard deviations) was obtained for the calculated SPR datasets in the anthropomorphic
126 head phantom.

127 To consider only voxels within the patient, an external contour was automatically created
128 based on the 80/140 kVp DECT scan using a threshold of -500 HU. This contour, covering
129 the patient surface, was subsequently shrunk by 3 (5) voxels in x (y) direction to exclude
130 remaining parts of immobilization devices. In scan direction, the datasets were restricted to
131 only include the head from chin to calvaria. Within this defined volume, the frequency
132 distribution of voxelwise correlations of two tissue parameters were determined, i.e., SPR and
133 RED depending on CT number H as well as EAN and RCS depending on RED as shown in
134 Figure 1.

135 The intra- and inter-patient variability was quantified based on the frequency distribution of
136 (H , SPR) correlations to assess the degree of non-uniqueness of a heuristic CT-number-to-
137 SPR conversion. The diversity of human soft tissues due to tissue mixtures and different
138 tissue types was characterized by the frequency-weighted average spread ω in SPR covering
139 95% of all CT voxels within the soft-tissue region ($-125 \text{ HU} \leq H \leq 75 \text{ HU}$):

$$\omega = \frac{1}{N_{\text{Total}}} \sum_H N(H) \cdot [p_{97.5, \text{SPR}}(H) - p_{2.5, \text{SPR}}(H)] \quad (1)$$

140 with N_{Total} as total number of voxels, $N(H)$ as number of voxels with respective CT number,
 141 $p_{x, \text{SPR}}$ as x th SPR percentile.

142 Within the bony region ($100 \text{ HU} \leq H \leq 1800 \text{ HU}$), the variation of slope α of an intensity-
 143 weighted linear regression within the (H, SPR) domain serves as measure for variations in
 144 human bones.

145 Significant variations between adults and children were assessed by two-sample t-tests with
 146 significance criterion of 5%.

147

148 *Compensation of systematic deviations in stopping-power prediction*

149 As previously demonstrated for brain-tumor patients, CT-based SPR prediction significantly
 150 differs between the application of an HLUT and a DECT-based DirectSPR method [21]. This
 151 results in a systematic global SPR and range deviation, which is very likely caused by tissue
 152 compositions and tissue distributions differing from HLUT calibration conditions [24].
 153 Hence, the SPR difference between the HLUT and DirectSPR approach is influenced by a
 154 combination of this systematic deviation as well as the intra- and inter-patient variability
 155 reflecting the ambiguity of the heuristic CT-number-to-SPR conversion. To isolate the
 156 influence of tissue variability on SPR prediction, the HLUT was adapted by minimizing the
 157 systematic deviation between both methods. For this purpose, the median SPR of each CT
 158 number was obtained from the frequency distribution of (H, SPR) correlations. Subsequently,
 159 the Hounsfield scale was divided in four classes corresponding to various tissue types: low-
 160 density ($-950 \text{ HU} \leq H \leq -160 \text{ HU}$), adipose ($-140 \text{ HU} \leq H \leq -40 \text{ HU}$), muscle and brain
 161 ($-20 \text{ HU} \leq H \leq 40 \text{ HU}$) as well as bone tissue ($100 \text{ HU} \leq H \leq 1800 \text{ HU}$). For each tissue
 162 class, the median SPR distribution was described by an intensity-weighted linear regression
 163 depending on the relative occurrence of the respective CT number within the patients. The

164 transitions between different classes were linearly connected, which finally resulted in the
165 cohort-specifically adapted HLUT.

166

167 *Assessment of SPR and range deviations*

168 The mean signed and absolute SPR deviation between both CT-based SPR prediction
169 approaches ($SPR_{HLUT} - SPR_{RhoSigma}$) was calculated including all CT voxels within the
170 patient's external contour. Tissue-dependent SPR differences were quantified using only CT
171 voxels of the respective tissue class as defined above.

172 To check whether the findings obtained on SPR level could be transferred to range deviations,
173 passively scattered proton treatment plans of two representative patients were recalculated on
174 SPR datasets derived from RhoSigma, clinical and adapted HLUT using XIO (Elekta AB,
175 Stockholm, Sweden) with a $1 \times 1 \times 1 \text{ mm}^3$ dose calculation grid. The distal range at 80% of
176 prescribed dose was determined for more than 5000 line-dose profiles in beam direction to
177 assess proton range shifts.

178

179 **Results**

180 *Tissue occurrence*

181 The investigated body region (head) mainly contains soft tissues (adipose, brain and muscles)
182 and bones with a mean fraction \pm one standard deviation between different patients of $(78.6 \pm$
183 $2.5)\%$ and $(18.9 \pm 2.3)\%$, respectively. The remaining, small fraction of apparent low-
184 density tissue of $(2.5\% \pm 0.5\%)$ is mostly caused by a sub-voxel mixture of air cavities and
185 various soft tissues or even bones.

186

187 *Soft tissue diversity*

188 As illustrated in Figure 1, children and adults showed a similar soft tissue distribution in all
189 physical quantities studied. The soft tissue region is dominated by brain ($H \approx 40\text{HU}$, $RED \approx$

190 1.034) and adipose tissue ($H \approx -100\text{HU}$, $RED \approx 0.920$). Even though, a broad SPR
191 distribution with a mean intra-patient SPR spread \pm one standard deviation of $\omega = (5.6 \pm$
192 $0.7)\%$ was found. This was induced by various tissue types, intra-tissue variations and
193 mixtures between brain and adipose tissue (indicated by a clearly visible line between the
194 tissue peaks) as well as between soft and low-density or bone tissues. The intra-patient SPR
195 spread within the soft tissue region differed significantly between children and adults ($p \ll$
196 0.001 , Figure 2). The increased soft tissue diversity in adults may potentially arise from the
197 large intrinsic variability within adipose tissues, e.g. the varying relative amount of lipids
198 from 61.4% to 87.3% [5], in combination with a slightly higher mean relative amount of
199 adipose tissue in adults ($16.5 \pm 4.0\%$) compared to children ($12.7 \pm 4.0\%$) (cf., equation 1).

200

201 *Variations in bone composition*

202 The distribution of bones differed between adults and children as indicated by a linear fit for
203 $SPR(H)$ and $RED(H)$ and power-function fit for $EAN(RED)$ and $RCS(RED)$ in Figure 1.
204 Bones in children revealed a smaller effective atomic number at same electron density and an
205 age-related significant reduction of the slope within the $SPR(H)$ domain (Figure 2), which are
206 presumably associated with a smaller relative amount of calcium embedded [5,25]. Since the
207 calcium content in bones increases with age, the influence of the photoelectric effect on CT
208 number also increases.

209

210 *Compensation of systematic SPR deviations*

211 To reduce systematic deviations in CT-number-to-SPR conversion, the HLUT was optimized
212 based on the DECT-derived SPR (Figure 3). The HLUT refinement was performed separately
213 for each patient cohort considering the difference in bone composition (Figure 2). The SPR
214 differences before (Figure 4A) and after HLUT adaptation (Figure 4B) for adults and children
215 demonstrated that a HLUT refinement can effectively compensate systematic deviations in

216 stopping-power prediction between the RhoSigma and HLUT approach. The HLUT
217 adaptation resulted in a significant reduction of systematic SPR deviations \pm one standard
218 deviation from $(2.0 \pm 0.6)\%$ to $(0.1 \pm 0.6)\%$ for low-density tissues, $(1.9 \pm 0.2)\%$ to $(0.1 \pm$
219 $0.2)\%$ for soft tissues, $(-2.4 \pm 0.9)\%$ to $(-0.3 \pm 0.7)\%$ for bones and $(1.1 \pm 0.3)\%$ to $(0.0 \pm$
220 $0.3)\%$ in total considering all 102 patients (Figure 5A).

221

222 *Residual intra- and inter-patient SPR variability*

223 After removing systematic deviations between the HLUT and RhoSigma approach, the
224 residual SPR deviations between both methods were assessed. The intra-patient SPR
225 deviations of a representative child and adult were comparable to SPR differences including
226 all patients within the respective cohort (Figure 4). The SPR variability within one patient
227 (e.g., $\omega = 5.6\%$ for soft tissues) is considerably larger than the variability between patients
228 (e.g., one standard deviation of ω is 0.7% for soft tissues). The broad distribution of SPR
229 deviations within adipose tissue (Figure 4) results in SPR differences up to 10% (relative to
230 the SPR of water), considering (H, SPR) correlations with a relative amount larger than
231 0.01% , and leads to a mean intra-patient SPR spread \pm one standard deviation of $\omega = (9.8 \pm$
232 $1.2)\%$ for adipose tissues only.

233 Despite the HLUT refinement, the intra-patient SPR variation remained almost unchanged in
234 soft tissues (Figure 4B). SPR variations in a single patient after (before) HLUT adaptation
235 translated into mean absolute SPR deviations of approximately 3% (4%) for low-density
236 tissues, 3% (6%) for bones as well as 1% (2%) for soft tissues. The latter corresponds to the
237 mean intra-patient SPR spread of $\omega = 5.6\%$ within soft tissues (Figure 5B). The large inter-
238 patient variation of SPR deviations in bones (Figure 5, interquartile range) illustrated the high
239 variability in bone composition between patients.

240

241

242 **Discussion**

243 The evaluation of DECT scans of 102 primary brain-tumor patients revealed a considerable
244 intra-patient soft tissue diversity leading to a broad SPR distribution with a frequency-
245 weighted average spread of $\omega = (5.6 \pm 0.7)\%$. However, this SPR spread does not only stem
246 from different tissue types, tissue mixtures and intra-tissue variability, but also from image
247 noise. The influence of image noise on SPR prediction was minimized by applying an
248 iterative image reconstruction algorithm at maximal strength. It was estimated as 1.2%
249 (relative to the SPR of water), which equals twice the image noise level (\pm two standard
250 deviations) of 6 HU in the calculated SPR dataset. This results in a noise-corrected mean SPR
251 spread of $\omega = 5.5\%$ (4.4%) using quadratic (linear) subtraction. This intra-patient SPR
252 variability in the soft tissue region is associated with a mean absolute SPR deviation between
253 the RhoSigma and HLUT approach of 1.2% (cf., Figure 5).

254 Furthermore, differences in bone composition between adults and children were observed. An
255 HLUT specified for adults would cause a SPR underestimation in bone of approximately 5%
256 for children younger than 6 years. To further validate the detected age-related changes in bone
257 composition, the investigated pediatric patient cohort may be extended in follow-up studies
258 allowing for a better age resolution. Additional studies may also analyze whether DECT can
259 further improve the quantification of senile osteoporosis in patients [26,27].

260 A refinement of the HLUT based on DECT-derived tissue information can on average reduce
261 the systematic global and tissue-specific SPR deviations between both CT-number-to-SPR
262 conversion methods. These systematic deviations originate from different tissue compositions
263 and distributions in patients as compared to the tissue surrogates used for HLUT specification
264 [24]. As exemplarily shown in Figure 6 for a representative child and adult, the mean relative
265 range deviation between RhoSigma and HLUT can also be reduced by applying the adapted
266 HLUT (Figure 6). However, depending on the tissues traversed in beam direction, CT-based
267 SPR prediction using either the adapted HLUT or RhoSigma can still result in range

268 differences of about 1% as illustrated by the standard deviation of the obtained range shifts
269 (Figure 6). The HLUT adaptation presented in this study was only based on the tissue
270 diversity within brain-tumor patients. In a further study, we are going to rather focus on the
271 irradiated volume of each patient including also immobilization devices. In addition, we also
272 consider patients with tumors located in other body regions such as thorax or pelvis to
273 comprehensively evaluate their influence on a HLUT refinement.

274 Within this study, the integral intra- and inter-patient variability of tissue properties were
275 determined in primary brain-tumor patients without distinguishing different organs or
276 anatomical structures. Further evaluations could individually assess the variability of specific
277 tissue types to update or supplement already existing patient tissue databases [5,25].
278 Moreover, the intra- and inter-patient variability of other body regions is to be evaluated (e.g.,
279 thorax and pelvis) to assess potential differences in tissue composition and distribution.

280

281 **Conclusions**

282 The presented investigation of the intra- and inter-patient SPR variability, as assessed in 102
283 primary brain-tumor patients using dual-energy CT for the first time, highlights a general
284 limitation of the state-of-the-art HLUT approach. The age-related bone variation (inter-patient
285 SPR deviations of roughly 5% between young children and adults) and the considerable soft
286 tissue variability in general (mean intra-patient SPR spread of 4-6% for a defined CT number)
287 cannot be fully accounted for by a generic HLUT. This leads to unavoidable deviations in
288 SPR prediction. The resulting contribution on SPR accuracy was so far only partly considered
289 in the uncertainty estimation of the HLUT approach and demonstrates a further advantage of a
290 DECT-based DirectSPR approach. Hence, an accurate patient-specific SPR prediction using
291 dual-energy CT is advisable for particle treatment planning, since it correctly handles tissue
292 mixtures and intrinsically incorporates most of intra- and inter-patient variability.

293 **Acknowledgments:**

294 This work was funded by the National Center for Radiation Oncology (NCRO) within the
295 project “Translation of dual-energy CT into application in particle therapy”.

296

297 **Conflict of Interest Statement:** The authors report no conflict of interest. OncoRay and
298 DKFZ have institutional research agreements with Siemens Healthineers.

299 **REFERENCES**

- 300 [1] Baumann M, Krause M, Overgaard J, Debus J, Bentzen SM, Daartz J, et al. Radiation
301 Oncology in the Era of Precision Medicine. *Nat Rev Cancer* 2016;16:234–49.
302 doi:10.1038/nrc.2016.18.
- 303 [2] Paganetti H. Range Uncertainties in Proton Therapy and the Role of Monte Carlo
304 Simulations. *Phys Med Biol* 2012;57:R99–117. doi:10.1088/0031-9155/57/11/R99.
- 305 [3] Knopf A-C, Lomax AJ. In vivo proton range verification: a review. *Phys Med Biol*
306 2013;58:R131–60. doi:10.1088/0031-9155/58/15/R131.
- 307 [4] Dinges E, Felderman N, McGuire S, Gross B, Bhatia S, Mott S, et al. Bone marrow
308 sparing in intensity modulated proton therapy for cervical cancer: Efficacy and
309 robustness under range and setup uncertainties. *Radiother Oncol* 2015;115:373–8.
310 doi:10.1016/j.radonc.2015.05.005.
- 311 [5] Woodard HQ, White DR. The Composition of Body Tissues. *Br J Radiol*
312 1986;59:1209–19. doi:10.1259/0007-1285-59-708-1209.
- 313 [6] Yang M, Virshup G, Clayton J, Zhu XR, Mohan R, Dong L. Theoretical Variance
314 Analysis of Single- and Dual-Energy Computed Tomography Methods for Calculating
315 Proton Stopping Power Ratios of Biological Tissues. *Phys Med Biol* 2010;55:1343–62.
316 doi:10.1088/0031-9155/55/5/006.
- 317 [7] Fattori G, Riboldi M, Scifoni E, Krämer M, Pella A, Durante M, et al. Dosimetric
318 effects of residual uncertainties in carbon ion treatment of head chordoma. *Radiother*
319 *Oncol* 2014;113:66–71. doi:10.1016/j.radonc.2014.08.001.
- 320 [8] Li H, Zhang X, Park P, Liu W, Chang J, Liao Z, et al. Robust Optimization in
321 Intensity-Modulated Proton Therapy to Account for Anatomy Changes in Lung Cancer
322 Patients. *Radiother Oncol* 2015;114:367–72. doi:10.1016/j.radonc.2015.01.017.
- 323 [9] Van Der Voort S, Van De Water S, Perkó Z, Heijmen B, Lathouwers D, Hoogeman M.
324 Robustness Recipes for Minimax Robust Optimization in Intensity Modulated Proton

- 325 Therapy for Oropharyngeal Cancer Patients. *Int J Radiat Oncol Biol Phys*
326 2016;95:163–70. doi:10.1016/j.ijrobp.2016.02.035.
- 327 [10] Stützer K, Lin A, Kirk M, Lin L. Superiority in Robustness of Multifield Optimization
328 Over Single-Field Optimization for Pencil-Beam Proton Therapy for Oropharynx
329 Carcinoma: An Enhanced Robustness Analysis. *Int J Radiat Oncol Biol Phys*
330 2017;99:738–49. doi:10.1016/j.ijrobp.2017.06.017.
- 331 [11] Flohr TG, McCollough CH, Bruder H, Petersilka M, Gruber K, Süß C, et al. First
332 Performance Evaluation of a Dual-Source CT (DSCT) System. *Eur Radiol*
333 2006;16:256–68. doi:10.1007/s00330-005-2919-2.
- 334 [12] van Elmpt W, Landry G, Das M, Verhaegen F. Dual Energy CT in Radiotherapy:
335 Current Applications and Future Outlook. *Radiother Oncol* 2016;119:137–44.
336 doi:10.1016/j.radonc.2016.02.026.
- 337 [13] Wohlfahrt P, Möhler C, Hietschold V, Menkel S, Greilich S, Krause M, et al. Clinical
338 Implementation of Dual-Energy CT for Proton Treatment Planning on Pseudo-
339 Monoenergetic CT Scans. *Int J Radiat Oncol Biol Phys* 2017;97:427–34.
340 doi:10.1016/j.ijrobp.2016.10.022.
- 341 [14] Hünemohr N, Krauss B, Tremmel C, Ackermann B, Jäkel O, Greilich S. Experimental
342 Verification of Ion Stopping Power Prediction from Dual Energy CT Data in Tissue
343 Surrogates. *Phys Med Biol* 2014;59:83–96. doi:10.1088/0031-9155/59/1/83.
- 344 [15] Bourque AE, Carrier J-F, Bouchard H. A Stoichiometric Calibration Method for Dual
345 Energy Computed Tomography. *Phys Med Biol* 2014;59:2059–88. doi:10.1088/0031-
346 9155/59/8/2059.
- 347 [16] Möhler C, Wohlfahrt P, Richter C, Greilich S. Range Prediction for Tissue Mixtures
348 Based on Dual-Energy CT. *Phys Med Biol* 2016;61:N268–75. doi:10.1088/0031-
349 9155/61/11/N268.
- 350 [17] Wohlfahrt P, Möhler C, Richter C, Greilich S. Evaluation of Stopping-Power

351 Prediction by Dual- and Single-Energy Computed Tomography in an Anthropomorphic
352 Ground-Truth Phantom. *Int J Radiat Oncol Biol Phys* 2018;100:244–53.
353 doi:10.1016/j.ijrobp.2017.09.025.

354 [18] Taasti VT, Michalak GJ, Hansen DC, Deisher AJ, Kruse JJ, Krauss B, et al. Validation
355 of proton stopping power ratio estimation based on dual energy CT using fresh tissue
356 samples. *Phys Med Biol* 2017;63:015012. doi:10.1088/1361-6560/aa952f.

357 [19] Bär E, Lalonde A, Zhang R, Jee K-W, Yang K, Sharp G, et al. Experimental validation
358 of two dual-energy CT methods for proton therapy using heterogeneous tissue samples.
359 *Med Phys* 2017. doi:10.1002/mp.12666.

360 [20] Möhler C, Russ T, Wohlfahrt P, Elter A, Runz A, Richter C, et al. Experimental
361 Verification of Stopping-Power Prediction from Single- and Dual-Energy Computed
362 Tomography in Biological Tissues. *Phys Med Biol* 2018;63:025001. doi:10.1088/1361-
363 6560/aaa1c9.

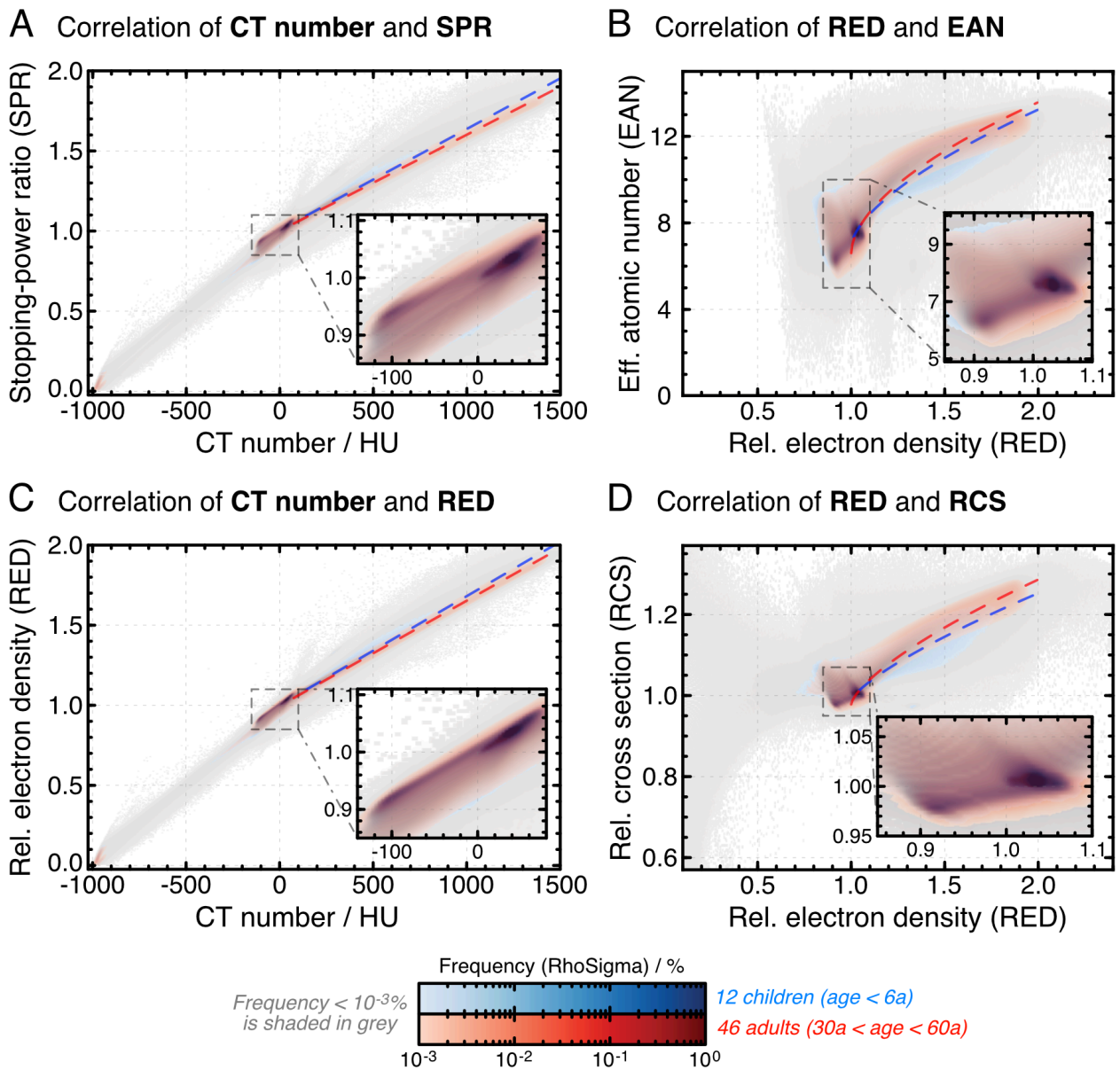
364 [21] Wohlfahrt P, Möhler C, Stützer K, Greilich S, Richter C. Dual-Energy CT Based
365 Proton Range Prediction in Head and Pelvic Tumor Patients. *Radiother Oncol*
366 2017;125:526–33. doi:10.1016/j.radonc.2017.09.042.

367 [22] Wohlfahrt P, Troost EGC, Hofmann C, Richter C, Jakobi A. Clinical Feasibility of
368 Single-Source Dual-Spiral 4D Dual-Energy CT for Proton Treatment Planning Within
369 the Thoracic Region. *Int J Radiat Oncol Biol Phys* 2018.
370 doi:10.1016/j.ijrobp.2018.06.044.

371 [23] Bethe H. Zur Theorie des Durchgangs schneller Korpuskularstrahlen durch Materie.
372 *Ann Phys* 1930;397:325–400. doi:10.1002/andp.19303970303.

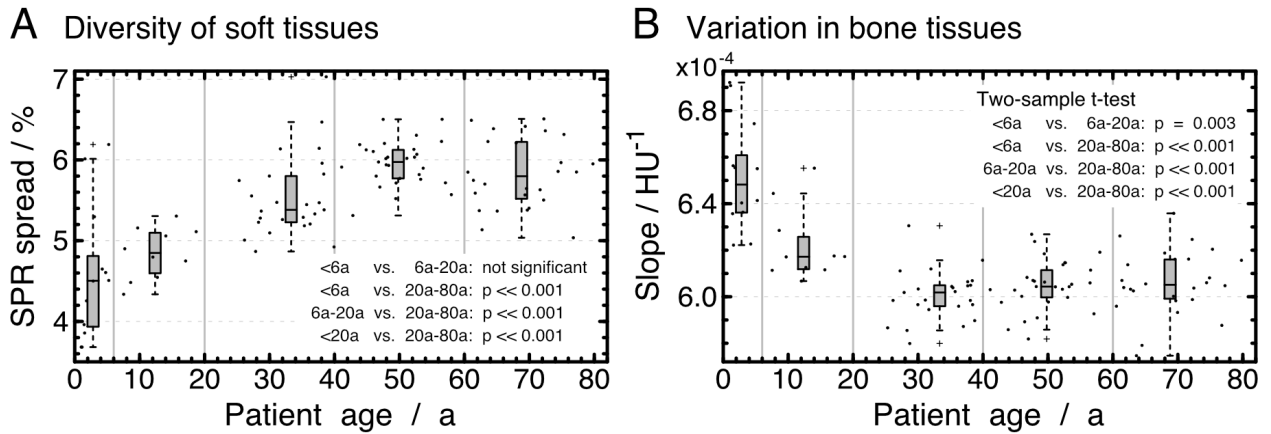
373 [24] Wohlfahrt P, Möhler C, Greilich S, Richter C. Comment on: Dosimetric Comparison of
374 Stopping-Power Calibration with Dual-Energy CT and Single-Energy CT in Proton
375 Therapy Treatment Planning [*Med. Phys.* 43(6), 2845-2854 (2016)]. *Med Phys*
376 2017;44:5533–6. doi:10.1002/mp.12418.

- 377 [25] White DR, Widdowson EM, Woodard HQ, Dickerson JWT. The Composition of Body
378 Tissues. (II) Fetus to Young Adult. *Br J Radiol* 1991;64:149–59. doi:10.1259/0007-
379 1285-64-758-149.
- 380 [26] Wichmann JL, Booz C, Wesarg S, Kafchitsas K, Bauer RW, Kerl JM, et al. Dual-
381 Energy CT–based Phantomless in Vivo Three-dimensional Bone Mineral Density
382 Assessment of the Lumbar Spine. *Radiology* 2014;271:778–84.
383 doi:10.1148/radiol.13131952.
- 384 [27] Booz C, Hofmann PC, Sedlmair M, Flohr TG, Schmidt B, D’Angelo T, et al.
385 Evaluation of Bone Mineral Density of the Lumbar Spine Using a Novel Phantomless
386 Dual-Energy CT Post-Processing Algorithm in Comparison with Dual-Energy X-ray
387 Absorptiometry. *Eur Radiol Exp* 2017;1:11. doi:10.1186/s41747-017-0017-2.
388



390

391 **Figure 1:** Frequency distribution of tissue parameters derived from dual-energy CT for
 392 children (blue) and adults (red). The superposition of both datasets appears purple. Dashed
 393 lines illustrate correlation in bony region.

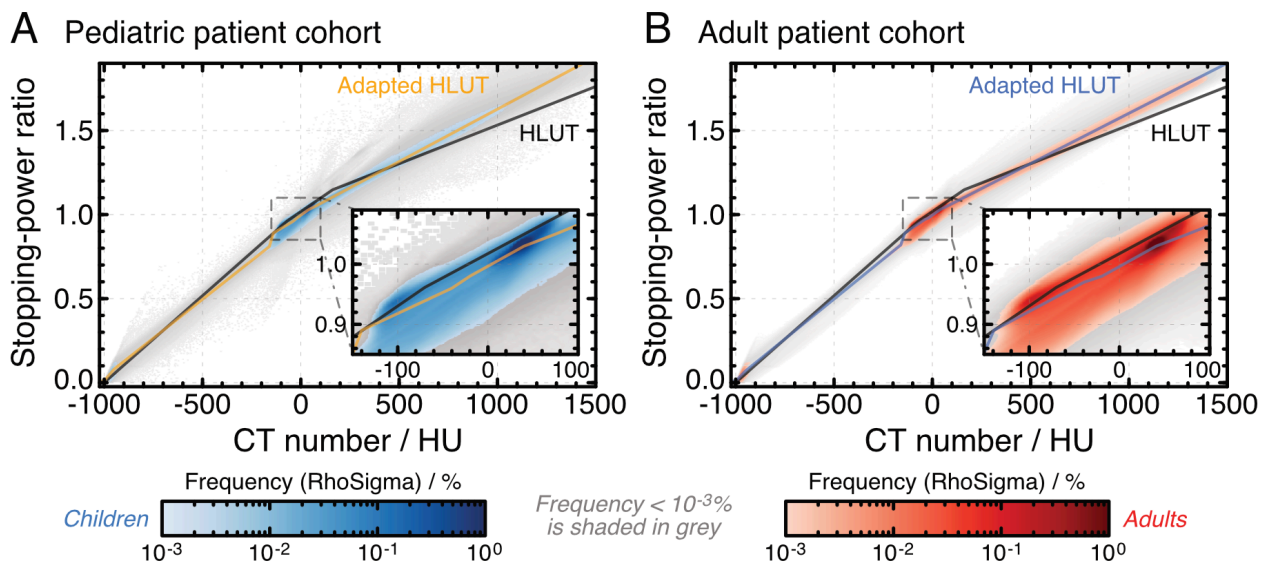


394

395 **Figure 2:** Age-related variation of (A) stopping-power ratio (SPR) spread in soft tissue (tissue
 396 diversity) and (B) the slope within bones (change in calcium content) for correlations between
 397 CT number and SPR. Patients were sorted in five groups depending on age (illustrated by
 398 vertical lines). Boxplots are defined according to Figure 5.

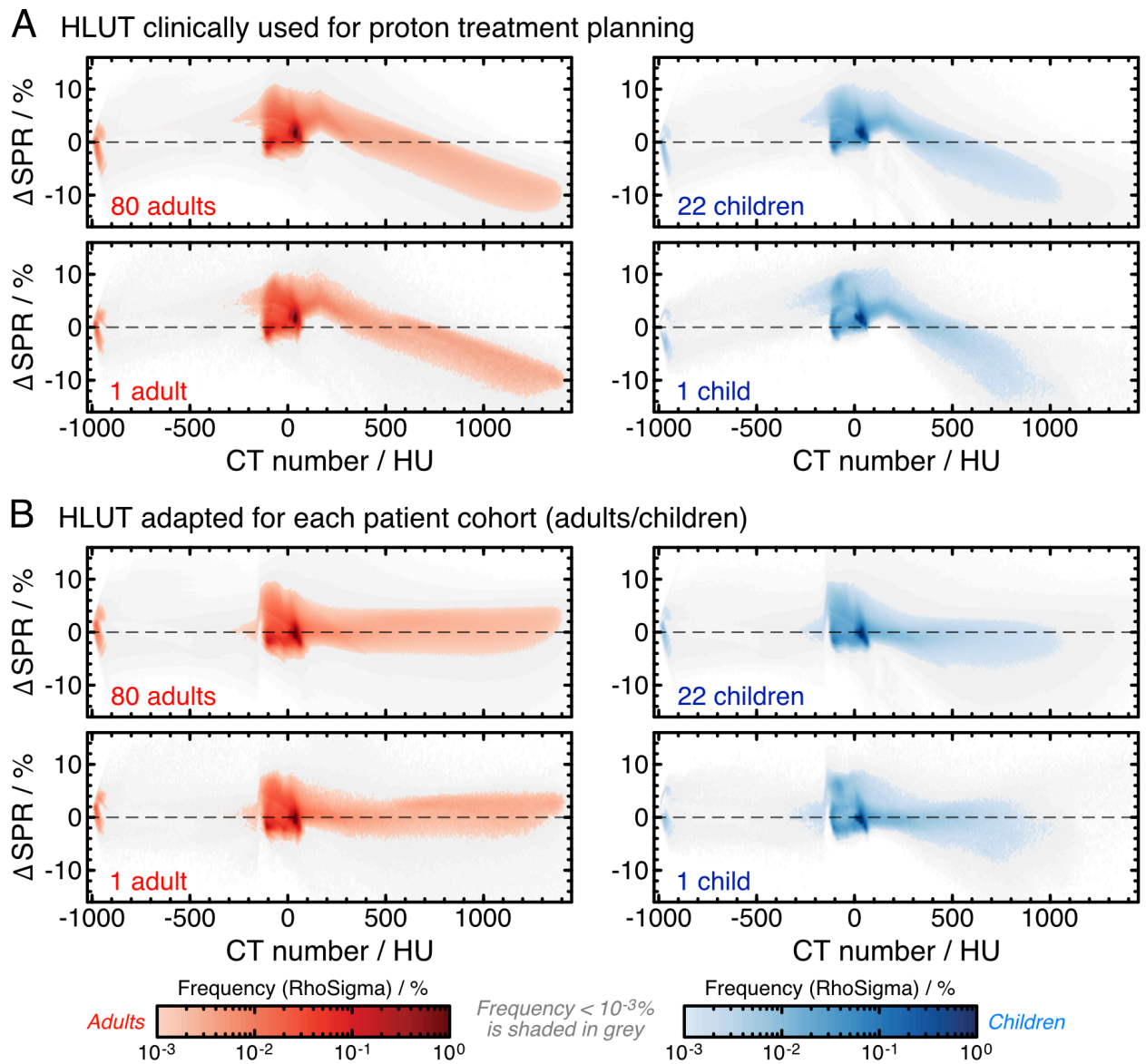
399

400



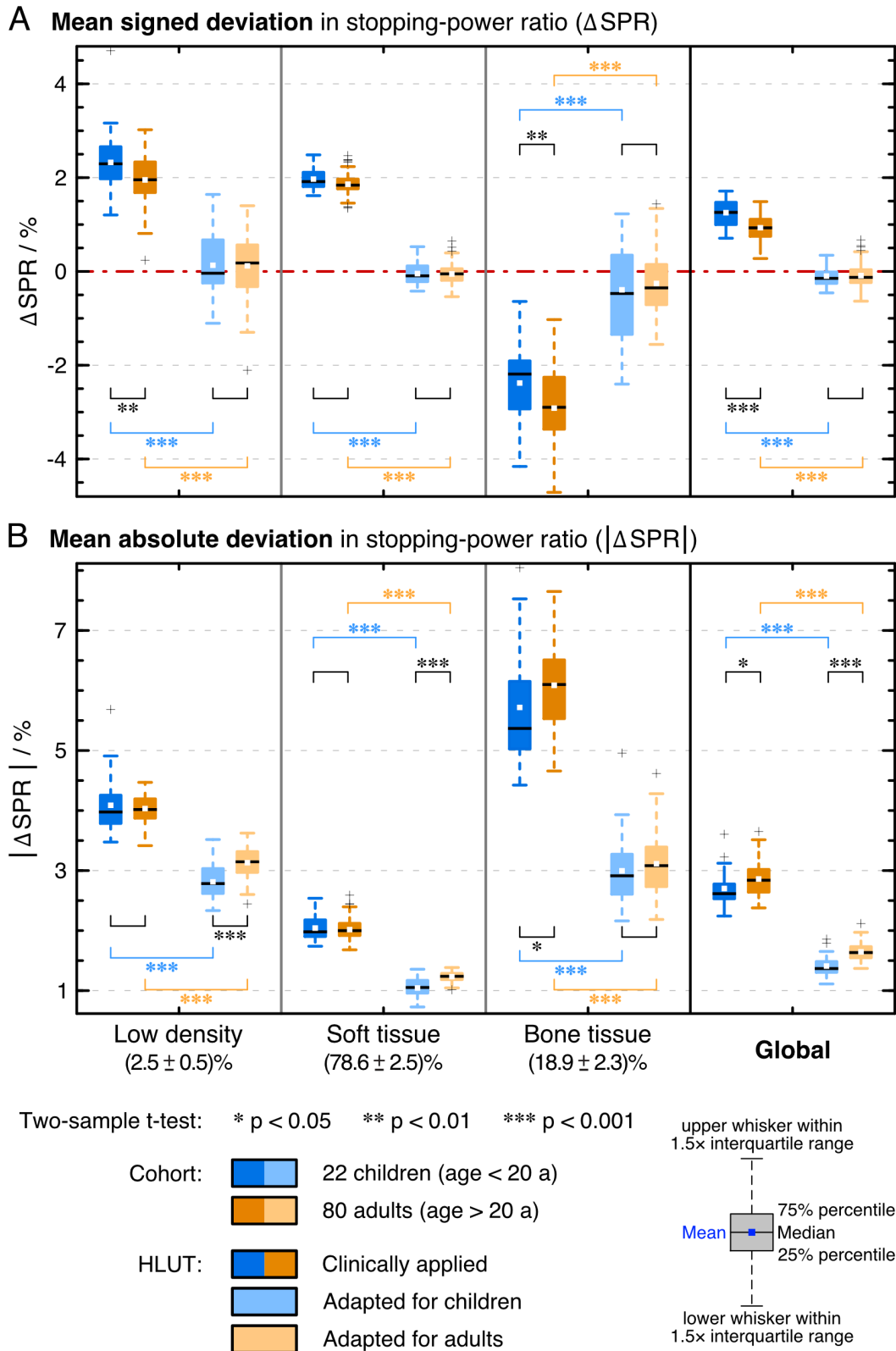
401

402 **Figure 3:** Frequency distribution of correlations between CT number and stopping-power
 403 ratio (SPR) for the (A) pediatric (younger than 20 years) and (B) adult patient cohort.



404

405 **Figure 4:** Difference in stopping-power ratio (SPR) between the dual-energy CT based SPR
 406 prediction (RhoSigma) and (A) clinically applied or (B) cohort-specifically adapted
 407 Hounsfield look-up table (HLUT) to visually compare the frequency distribution in one
 408 patient with the entire patient cohort. The colored (grey-shaded) frequency distribution covers
 409 all correlations with a frequency larger (lower) than $10^{-3}\%$.



410

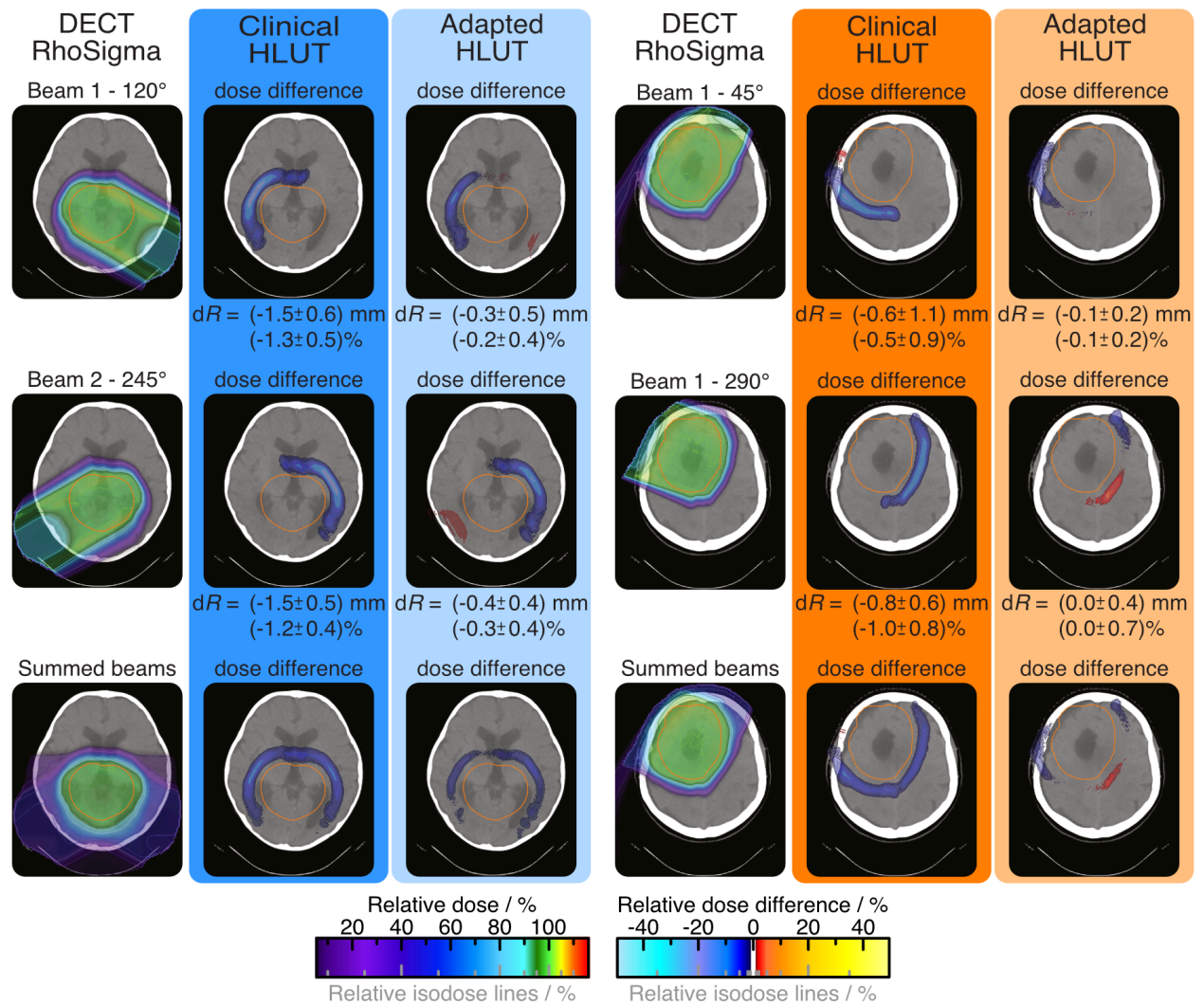
411 **Figure 5:** Global and tissue-specific mean (A) signed and (B) absolute SPR deviation

412 between the dual-energy CT based SPR prediction and clinically applied or adapted

413 Hounsfield look-up table (HLUT). The relative amount is quoted for each tissue type below.

A Treatment plan of a 3-years old child

B Treatment plan of an adult



414

415 **Figure 6:** Dose difference as well as mean absolute and relative range deviation (dR) between
 416 the dual-energy CT based stopping-power prediction and clinically applied or adapted
 417 Hounsfield look-up table (HLUT) for two single treatment fields and the summed treatment
 418 plan.

419 **FIGURE CAPTIONS**

420

421 **Figure 1:** Frequency distribution of tissue parameters derived from dual-energy CT for
422 children (blue) and adults (red). The superposition of both datasets appears purple. Dashed
423 lines illustrate correlation in bony region.

424

425 **Figure 2:** Age-related variation of (A) stopping-power ratio (SPR) spread in soft tissue (tissue
426 diversity) and (B) the slope within bones (change in calcium content) for correlations between
427 CT number and SPR. Patients were sorted in five groups depending on age (illustrated by
428 vertical lines). Boxplots are defined according to Figure 5.

429

430 **Figure 3:** Frequency distribution of correlations between CT number and stopping-power
431 ratio (SPR) for the (A) pediatric (younger than 20 years) and (B) adult patient cohort.

432

433 **Figure 4:** Difference in stopping-power ratio (SPR) between the dual-energy CT based SPR
434 prediction (RhoSigma) and (A) clinically applied or (B) cohort-specifically adapted
435 Hounsfield look-up table (HLUT) to visually compare the frequency distribution in one
436 patient with the entire patient cohort. The colored (grey-shaded) frequency distribution covers
437 all correlations with a frequency larger (lower) than $10^{-3}\%$.

438

439 **Figure 5:** Global and tissue-specific mean (A) signed and (B) absolute SPR deviation
440 between the dual-energy CT based SPR prediction and clinically applied or adapted
441 Hounsfield look-up table (HLUT). The relative amount is quoted for each tissue type below.

442

443 **Figure 6:** Dose difference as well as mean absolute and relative range deviation (dR) between
444 the dual-energy CT based stopping-power prediction and clinically applied or adapted

445 Hounsfield look-up table (HLUT) for two single treatment fields and the summed treatment
446 plan.